Research Square

Preprints are preliminary reports that have not undergone peer review.
They should not be considered conclusive, used to inform clinical practice,
or referenced by the media as validated information.

Biological Assessment of Wet-Chemically Prepared SnO_2 Nanoparticles: Evaluating Antimicrobial Response and SKMEL Melanoma Cytotoxicity

Krishnamoorthy Nanjundan

yenkrish.spectrum@gmail.com

Sri Eshwar College of Engineering

Indhumathi Kamaraj

Dr. N.G.P. Arts and Science College

Gladya Anusha. A

Christuraja Matriculation Higher Secondary School

Research Article

Keywords: SnO2 NPs, co-precipitation, antibacterial activity, cytotoxicity, Raman spectrum, PL emission

Posted Date: September 23rd, 2026

DOI: https://doi.org/10.21203/rs.3.rs-10978477/v1

License: This work is licensed under a Creative Commons Attribution 4.0 International License. Read Full License

Additional Declarations: No competing interests reported.

Abstract

The increasing interest on tin oxide nanoparticles due to its properties and biological activity may have promising application in the biomedical field. In the present work, SnO_2 nanoparticles (NPs) synthesized via a co-precipitation method with aqueous ammonia as precipitating agents, both with and without addition of the surfactant Triton X-100 followed by a calcination process was developed. Structural characterization, morphology, elemental composition, chemical surface nature, optical properties, and the thermal stability of SnO_2 NPs were investigated by utilizing XRD, SEM-EDS, FTIR, Raman, PL, and TGA. Antibacterial studies against six different strains were investigated by the agar well-diffusion method. The highest inhibition zone was found against Klebsiella pneumoniae (12 mm for S4), and inhibition range of Staphylococcus aureus was 9 mm for S1 and S3 respectively. In vitro cytotoxicity activity against SKMEL melanoma cells showed concentration dependent of cell mortality and S4 exhibited the higher activity with an IC_{50} is 66.96 µg/mL, and followed by S3 (95.57 µg/mL). We hypothesize that surface defects may drive bioactivity and the research also suggests that the synthesis condition affect the material physico-chemical and bioactivity properties and provide the base for subsequent application of SnO_2 NPs.

1. Introduction

Over the last decade; researchers have devoted immense effort in producing metal oxide semiconductor (MOS) nanomaterials due to their unique chemical and physical characteristics as well as their vast applications, ranging from electronics to biomedical materials (Hossain et al. 2023; Kamaraj et al. 2025; Hughes et al. 2025; Bamisaye et al. 2025). Amongst these, SnO nanoparticles are widely used for their excellent combination of properties, e.g. their high electrical conductivity, remarkable transparency in the visible spectrum, as well as high chemical and thermal stability along with their good sensing ability for gases (Kharbanda et al. 2022; Sharma et al. 2021; Sagadevan et al. 2021; Rahman et al. 2025).

Tin forms several types of oxides; among which only two are well established and well known namely SnO_2 and SnO; both containing Sn at the same oxidation states of 4 + and 2+, respectively. Since SnO_2 is thermodynamically stable under an oxidizing ambient environment it usually crystallizes in the tetragonal structure (space group P4 2/mnm) which features typical rutile like lattice parameters with the values as reported before to be a = 4.738; c = 3.187 (Sharma et al. 2021). This n-type semiconductor nature is associated with a large bandgap value of approximately 3.6-4.0 eV and electrical conductivity of SnO_2 can be tuned via controllable oxygen vacancy formation by tailoring specific synthesis parameters (Mohanta et al. 2016; Wang et al. 2016). Due to these beneficial properties, it is not surprising that, over recent years, SnO_2 nanostructures have been explored for a vast scope of technologies including: (i) energy conversion and storage (where high electron mobility, makes it a very good photoanode for solar cells (Wali et al. 2015; Dalapati et al. 2021), and high theoretical capacity makes it very attractive as an anode material in lithium-ion batteries (Lan et al. 2022; Kebede et al. 2020) and its pseudocapacitive response good as electrode material in supercapactitors (Zhao et al. 2015); (ii) gas sensing (highly sensitive to reducing gases like H_2, CO, VOCs (Masuda et al. 2022; Shanmugasundaram et al. 2024; Li et al. 2022) and (iii) photocatalytic degradation of environmental pollutants (under UV radiation through photo-separation of charges and subsequent re-

distribution of radicals at the surface of the material (Sun et al. 2022; Hussain et al. 2025; Alamdari et al. 2026).

In the biomedical arena, SnO_2 nanoparticles have gained significant attention (Khan et al. 2025; D'Souza et al. 2025) and recent studies revealed significant activity towards both Gram +ve and Gram -ve bacteria, through diverse proposed mechanisms; the proposed mechanism for antibacterial action includes either surface induced damage or through the production of reactive oxygen species (ROS) with eventual oxidative stress on the biological entities (Kishorwara et al. 2026; Khan et al. 2025; Bamagous et al. 2025; Dharmaraja et al. 2017; Van Acker and Coenye 2017; Imlay et al. 2013).

The proportion at which individual ROS species play the dominant role would vary depending on specific material composition and laboratory conditions and the relation to oxygen vacancies. SnO_2 nanoparticles were also tested for their efficiency against cancerous cells though more evidence is needed on cancer selective cell death versus normal cell counterparts (Chandrasekaran et al. 2024; Akter et al. 2026; NavaneethaKrishnan et al. 2019; Alzahrani et al. 2023; Shinde et al. 2022).

Also enhancement through an EPR mechanism has been proposed to allow tumor specificity of the particle aggregation with a particular focus in enhanced permeability and retention effects in tumor tissues (Shinde et al. 2022). Several methods are available for nanostructured SnO_2. For example, the Sol-Gel method has the advantage in being size and morphology controllable, while yielding a good quality nano-material but it requires prolonged reaction times and expensive precursors (Kumar et al. 2025; Gebreslassie et al. 2021); Microwave assisted techniques lead to the synthesis of nano-materials having controlled size distributions through very short heating times (Manimaran et al. 2023).

Hydrothermal and solvothermal methods allow one to get high purity and crystalline nano-materials but are time consuming and require high pressure reactors (de Conti et al. 2023). The sonochemical method is capable of producing stable and high energy metastable phases though the reaction rate would depend on the acoustic parameters of the ultrasonic source (Agadi et al. 2023). The mechanochemical synthesis route being simple, scalable and cost effective can produce impurities and low purity of the products (Billik et al. 2009). Among different method co-precipitation was chosen for its promising characteristics such as high yield and process ease. It is a cheap method and requires the preparation of a metal hydroxide/carbonate species that is finally calcined to the corresponding oxide.

Key advantages for this method are (1) it operates at standard temperature and pressure conditions; (2) it can be carried out in the simplest laboratory equipment; (3) particle size and morphology are tunable using reagent concentration and solution pH; (4) the precipitant is normally removed by adequate washing, leading to a purified nano-material; (5) minimal experimental time for the synthesis procedure to be completed.

These advantages lead to the selection of this method in the present study, since the quality of the nanostructured material along with process scalability is expected to be extremely important for their eventual use as biomaterial (Zhao et al. 2023; Nasir et al. 2017; John et al. 2018). Despite the extensive literature available on SnO_2 nanoparticles and their specific uses there is still a lack of relation to be established among the conditions of the preparation parameters, the physico-chemical characteristics of the resulting nano-material and eventually their biological behaviour. In particular the relationship between these

preparation conditions and cell killing efficiencies and bacterial growth inhibiting effect for a different range of synthesis precursors/precipitants is yet to be determined.

For these reasons, in the present study we would: (1) synthesize SnO_2 nanoparticles by different precipitant based co-precipitation. (2) characterize each sample by different relevant techniques for determination of its structure, morphology, chemical state, optical as well as thermal features to correlate physical parameters with biological characteristics in order to deduce whether a relation exists among them; (3) investigate their antibacterial behaviour on Gram +ve and Gram -ve bacteria strains; (4) study their cytotoxic/cytostatic effect toward human SKMEL melanoma cells by determining the corresponding IC_{50} for a cell to dose ratio. We assume that variation of synthesis parameters would induce different material properties which in turn can affect biological function.

2. EXPERIMENTAL DETAILS

2.1. Materials

All chemicals that were applied in this experiment were analytical grade reagents and further applied without additional purification or additional purifications process. Stannous chloride dihydrate ($SnCl_2.2H_2O$, 99% purity), NH_4OH (25% w/w), Triton X-100 chemicals were obtained from Merck, India. For all the operations, distilled water of 2.8 μS/cm was used. Ethanol of high purity level of 99.9% was utilized to wash. All bacteria culture media like Mueller-Hinton (MH) agar, nutrient broth and antibiotic discs (Gentamycin) were purchased from HiMedia Laboratories. Bacteria cultures: SKMEL melanoma cell line was purchased from National Centre for cell science (NCCS), Pune, India. DMEM (Dulbecco's Modified Eagle Medium), FBS (fetal bovine serum), Penicillin-streptomycin and MTT (3-(4,5-Dimethylthiazol-2-yl)-2,5-diphenyl tetrazolium Bromide) were purchased from HiMedia laboratories.

2.2. Synthesis of SnO_2 Nanoparticles

Simple co-precipitation was used to synthesize SnO_2 nanoparticles using $SnCl_2{\cdot}2H_2O$ as the tin source with the precipitating agent Aqueous NH_3 (25%) (Anil et al. 2024). Deionized water (whose electrical conductivity was measured to be 2.8 μS cm^{-1}, was employed as solvent (Das et al. 2020). Reagents were of analytical grade and were used as received. 2.256 g (0.01 mol) $SnCl_2{\cdot}2H_2O$ was dissolved in 100 mL deionized water and stirred magnetically at room temperature for 30 min until a completely homogeneous and transparent precursor solution was obtained. Exactly10 mL of aqueous solution (NH_3, 25%) was added drop by drop to the stirring precursor solution until pH = 10 and a white precipitate of tin hydroxide was obtained (Balakrishnan and OICC Author 2024). The suspension was stirred for a further 2 h to ensure complete precipitation and nucleation. The mixture was then aged overnight at room temperature without disturbance. The precipitated samples were obtained through filtration and were sequentially washed with deionized water and ethanol for removal of residual chloride ions and other reactants. The purified precipitate was dried under a hot-air furnace at 80°C for 4 h and the dried powder obtained at this step, was designated as Sample S1. A portion of the dried powder was placed in a muffle furnace and annealed at 600°C for 2 h, at a heating rate of 5^o C min^{-1} under air. The calcined sample was allowed to cool naturally to room temperature and designated as Sample S2.

2.3. Synthesis of Triton X-100-Assisted SnO_2 Nanoparticles

In this surfactant mediated synthesis technique, a similar co-precipitation method has been used and the only modification included here is the addition of a non-ionic surfactants named Triton X-100. Before precipitation of the tin precursors was initiated, Triton X-100 was slowly poured into the homogeneous precursor solution equivalent to 5 volume % of the precursor solution and simultaneously it was stirred via magnetic stirrer. The mixture was stirred at the same condition for 30 minutes for proper mixing. Then, 10 ml NH_4OH solution was added dropwise under continued stirring, up to pH 10 to yield a white precipitate.

The slurry was stirred for 2 h. Then the mixture was kept standing over night. It was filtered and rinsed repeatedly with deionized (DI) water and Ethanol. The resultant solid was collected and oven dried at 80° C for 4 h and labelled as sample S3, where one part of sample S3 was again heated at 600°C for 2 h using a muffle furnace in air. The cooled resulting product at room temperature was designated as Sample S4. A schematic presentation of procedures carried out is presented in Fig. 1. With inclusion of NH_4OH, hydroxide ions are produced that readily come into contact with Sn ions to form the tin hydroxide precipitate. The role of Triton X-100 is to influence (via its surfactant mechanism of action on precursor and nuclei), the processes of nucleation and growth, and it is not directly involved in the general stoichiometric reaction (Liang et al. 2019).

2.4. Characterization Techniques

2.4.1. X-ray Diffraction (XRD)

The structure of the crystal and the purity of the phase for the prepared SnO_2 nano-particles were identified with X-ray Diffraction (XRD) analysis. The X-ray diffractometer was operated with 40 kV voltage and 30 mA current in Cu Kα radiation (λ = 1.5406 Å). Data were obtained by using 2θ range of 20-80^o with a 0.02 step size and 2^o/min scan speed. The crystalline phase of the SnO_2 NPs was identified using X-ray data from the Joint Committee on Powder Diffraction Standards (JCPDS) database and the size of crystallites (D) was estimated from peak line broadening with use of the Debye Scherrer equation (Sultana et al. 2023):

$$D = \frac{K\lambda}{\beta \cos\Theta} \quad (1)$$

where, K is the shape factor (0.94 for spherical crystallites), λ is the wavelength of Cu Kα radiation (1.5406 Å), β is the full width at half maximum of the diffraction peak in radians and θ is the Bragg diffraction angle.

2.4.2. Scanning Electron Microscopy (SEM) and Energy-Dispersive X-ray Spectroscopy (EDAX)

The surface morphology and microstructure of the SnO_2 nanoparticles were examined at an accelerating voltage of 10–20 kV. The samples were prepared by dispersing the powder in ethanol through ultrasonication for 10 minutes and drop-casting onto carbon tape-coated aluminum stubs (Tripathy et al. 2022). SEM images were acquired at various magnifications to reveal surface features, grain size and morphology. The elemental composition and purity of the nanoparticles were determined using EDAX attached to the SEM. EDAX spectra

were collected from multiple areas of each sample to ensure representativeness. The atomic percentages of Sn, O and any impurity elements were quantified using the ZAF correction method (Pathak et al. 2020).

2.4.3. Fourier-Transform Infrared Spectroscopy (FTIR)

FTIR spectra were used to characterize the surface chemistry and functional groups of SnO_2 nanoparticles. The FTIR spectra were recorded in the wavenumber region of 400–4000 cm^{-1}. In the preparation of the KBr pellet, 1 mg of nanopowder was ground finely with 100 mg of spectral-grade KBr and pressed under 10 tons of pressure. The FTIR was performed at scanning range and resolution of 4 cm^{-1} and 64 scans respectively to obtain improved signal to noise ratio (Silva et al. 2016). A pure KBr pellet was used for background correction and subtraction prior to recording the spectra of the samples.

2.4.4. Photoluminescence Spectroscopy (PL)

PL spectra of the SnO_2 nanoparticles were recorded using a xenon lamp as the excitation source at room temperature. Each sample was dispersed in ethanol at 0.1 mg/mL dispersion, the sample was placed into the quartz cuvette (1 cm path length) and excited with a xenon lamp source at room temperature with excitation wavelength set at 325 nm (3.81 eV), then the emission spectra were recorded between 350–650 nm at spectral resolution of 1 nm (Gour and Kumar 2021). It should be noted that all the measurements were performed at room temperature.

2.4.5. Thermogravimetric Analysis (TGA)

Thermogravimetric analysis (TGA) was performed to evaluate the thermal stability and decomposition nature of the prepared nanoparticles. Around 10 mg of each powder was placed in a platinum crucible and heated from ambient temperature to 1000° C at a heating rate of 10°C/min in a flow of inert nitrogen gas at the rate of 50 mL/min. Differential thermal analysis was employed to determine the endothermic and exothermic transitions of the materials along with TGA. Weight loss was measured against temperature and derivative TGA to recognize the temperature associated with maximum weight loss (Gour and Kumar 2021).

2.5. Antibacterial Activity Evaluation

Synthesized SnO_2 NPs were screened against the six clinical strains which included three gram-positive bacteria; Staphylococcus aureus (ATCC 25923/MTCC 87) and Bacillus subtilis (ATCC 6633/MTCC 2413), and three gram-negative bacteria; Escherichia coli (ATCC 25922/MTCC 443), Pseudomonas aeruginosa (ATCC 27853/MTCC 741), Klebsiella pneumonia (ATCC 700603/MTCC 3384), and Vibrio cholera (ATCC 39315/MTCC 3906) strains based on the antibacterial effects (Vidhu and Philip 2014). The selected strains were kept at 4^oC in nutrient agar slants and sub-cultured at least every two weeks to retain viability. In the experiment, each bacteria strain was incubated at 37^oC for 24 h in nutrient broth at 37^o C for growth to attain the log phase cultures. The log phase bacterial cultures were diluted to the O. D. Of 0.5 Mc Farland standards (approximately $1.5X10^8$ CFUs/mL) using sterile saline (0.9% NaCl).

The screening for antibacterial activities of the sample was done by the agar well diffusion method as per by guidelines from CLSI (CLSI 2020).For screening of antibacterial activity, M-H agar plates were prepared, the medium consisted of 38 gm of commercially dehydrated M-H agar powder (M/s Himedia, India) per 1 Liter distilled water. The mixture was then autoclaved for 15 minutes at 121^o C at 15 PSI and about 20 ml of the

dispersed media poured onto sterile Petrie dishes. Agar plates were kept aside to allow hardening and drying at room temperature. Each plate was inoculated with 0.1 ml of standardized bacterial suspension (~ 10^8 CFU/mL) spread evenly using sterile cotton swab ensuring complete coverage of surface of agar plate. A 7 mm diameter Agar well was created in each plate by sterile cork borer and 100 µL of synthesized nanoparticles suspension (10 mg/mL concentration prepared by using distilled water; i.e., 100 µg per well) was added to each well. Nanoparticles suspension was prepared fresh and then sonicated for 10 minutes to get a homogenous suspension. The negative control well was added with distilled water and the positive control well was added with Gentamycin (160 µg/mL, 40 µL from 4 mg/mL) as standard antibiotic (Fatima et al. 2021). Plates were incubated at 37^o C for 24 hrs. The zone of inhibition was measured in mm and results were averaged from three replicates as mean standard deviation.

2.6. Anticancer Activity Evaluation

The anticancer activity of SnO_2 nanoparticles were evaluated against SKMEL cells by MTT assay. SKMEL cells were cultured with 10% heat inactivated FBS containing medium supplemented with 100 U/mL penicillin, 100 µg/mL streptomycin, 2mM L-glutamine and incubated in a humidified 5% CO_2 atmosphere at 37° C (Sultana et al. 2023). The SKMEL cells (2500 cells/well) were cultured into a 96 well plate with DMEM containing 10% heat inactivated FBS containing medium and were incubated for 24 hours to equilibrate the atmosphere in media.

The test samples were prepared in DMEM media at 100 µg/mL. The test samples dissolved in media were filtered using 0.2 µm Millipore syringe filter to make the samples free of contaminants and introduced to the cells at various concentrations of 6.25, 12.5, 25, 50, 100 µg/mL and control wells were maintained for wells without test samples. All experiments were conducted in triple so as to minimize the errors and to analyse accuracy. The plate was incubated for 24 hours at 37^o C in a humidified 5% CO_2 atmosphere to facilitate the test samples to reach cells and interact. After incubation, the media from the wells was aspired out and replaced with 100 µL of 0.5 mg/mL MTT solution in PBS. The plate was kept for incubation of 2 hours for the development of formazan crystals. The supernatant was removed, and then 100 µL of DMSO (100%) was added to each well in order to solubilize formazon crystals. The absorbance was measured with an ELISA plate reader at 570 nm. To check consistency, two wells were included in each plate without the cell sample as blank. Cell viability was calculated by taking the average absorbance from the treated and control group using the formula:

$$\text{Percentage of cell viability} = \left(\frac{\text{Average absorbance of treated}}{\text{Average absorbance of control}}\right) \times 100 \quad (2)$$

IC_{50} values (half maximal inhibitory concentration) were determined using four-parameter logistic curve fitting in Graph Pad Prism 8.0 and also calculated using the equation for slope (y = mx + C) obtained by plotting the average absorbance of the different concentrations of the test sample (6.25–100 µg/mL) in Microsoft Excel. All experiments were conducted in triplicate and data were presented as mean SD. The values were assessed statistically by one-way ANOVA accompanied by Dunnett's post hoc test and were considered as statistically significant if the value of $p < 0.05$ (Gour and Kumar 2021).

3. RESULTS AND DISCUSSION

3.1. Crystal Structure and Phase Identification

The crystallinity and the phase purity of the synthesized SnO_2 nanoparticles were characterized by XRD. The XRD pattern of all the four synthesized samples (S1-S4) in the 2θ range 20-80^o are shown in Fig. 2. The diffraction pattern showed sharp and well-defined peaks, signifying a highly crystalline nature of the nanoparticles.

All of the observed diffractions were successfully indexed to a tetragonal rutile structure of SnO_2 with lattice parameters of a = 4.738Å and c = 3.187Å, which match the values of ICDD card No. JCPDS/PDF 41-1445very well. The most intense diffraction peaks at 2θ value of 26.61^o and others observed at 33.89 ^{o}, 37.95 ^{o}, 51.78 ^{o}, 54.76 ^{o}, 61.87 ^{o}, 63.45 ^{o} and 65.94 ^{o} correspond to the (110), (101), (200), (211), (220), (310), (112), (301) and (202) crystal planes (Azam et al. 2012; Kashyap et al. 2023). For the SnO_2 phase, the (110) peak at 26.61^o is the highest peak intensity for all the samples, which may indicate that the (110) plane is the preferred orientation of the SnO_2 crystals. In SnO_2 single crystals, (110) plane is the facet with the minimum surface energy, and thus, tends to develop in most of the polycrystals. This face would be the dominant one, contributing the most surface fraction to the total surface area followed by other faces for a well-crystallized SnO_2 sample.

The absence of secondary peaks indicated that the entire tin hydroxide precursor was fully transformed to the phase pure SnO_2 after calcination at 600° C and the synthesized nanoparticle was highly pure. Least-squares method refined lattice parameters agree with the values of the tetragonal rutile structure. The small variations in refined lattice parameters between the samples could arise from variations in lattice strain and oxygen vacancy concentration. Average crystallite sizes were calculated from FWHM of the major diffraction peak by the use of Debye-Scherrer equation. Crystallite sizes are observed to range between 14.5 nm for the S2 calcined sample, and 23.0 nm for the S4 sample. The larger size for the samples prepared under Triton X-100 influence is assumed to be due to changes in crystal growth and nucleation process. Thermal treatment generally leads to crystallite growth and particle coalescence whereas the surfactant mediation might affect the beginning conditions for the crystal growth. Here, Triton X-100 has been employed as a templating agent. Triton X-100 may promote a uniform porous structure during precipitation; however, this structure may not remain stable at 600° C, where thermal treatment can cause grain growth and coalescence through the decomposition and removal of residual hydrocarbonaceous species. As far as the uncalcinated S3 is concern, still a moderate value for crystallite size was existed (21.0 nm), that might indicate the guiding effect on the nucleation rather than on aggregated growth of crystallites on particle after the decomposition.

3.2. Surface Morphology and Microstructure

The morphology of the synthesized SnO_2 nanoparticles, in particular the microstructures on its surface was characterized using field-emission scanning electron microscopy (FE-SEM). For all micrograph studies, the applied accelerating voltage (EHT) was 10.00 kV whereas the working distance (WD) was maintained at 8.5

mm by using the secondary electron (SE1) detector, so that increased topographic information is provided (See Fig. 3).

The SEM images of sample S1 (Fig. 3a) show predominantly spherical to polyhedral grains with a wide size distribution ranging from 100–400 nm. The particles appear to be significantly agglomerated as a common phenomenon in nanoparticles due to their high surface energy. The surface of the grains appears relatively smooth though some initial porosity is visible. Surface cracks and irregularities are visible in the SEM images; however, specific crystallographic defects such as twins or stacking faults cannot be conclusively identified from SEM alone. The presence of twins or stacking faults are evident as cracks on the grain surfaces. They are typical of rutile SnO_2 that result from the accommodation of lattice strain during crystal growth (Wang et al. 2013). The grain boundaries are clearly defined indicating good crystallinity despite the agglomeration.

Sample S2 (Fig. 3b) calcined at 600°C exhibits a more homogeneous grain size distribution with particle sizes ranging from 80–300 nm. The morphology is predominantly spherical though some elongated or rod-shaped particles are visible. This morphology may be associated with anisotropic growth, although preferred growth direction cannot be established conclusively from SEM alone. The morphology suggests that calcination at 600°C promotes particle coalescence and produces more consolidated structures. The surface is characterized by a fine porous structure and fine visible crystallites confirming the existence of polycrystalline aggregation grains.

The addition of the non-ionic surfactant Triton X-100 to S3 produced particles with a size range of approximately 100–350 nm and a more textured surface. The observed morphology is consistent with a possible surfactant-mediated influence on nucleation and growth; however, claims of mesoporosity or a templating mechanism require complementary surface-area and pore-size measurements (Üstünel et al. 2023; Zhao et al. 2018). Sample S4 (Fig. 3d) is produced using surfactant assistance at followed by a calcination step at 600°C, revealing the most uniform spherical-shaped to somewhat ovoid morphology and well-formed surface with sharp edges and uniform particle dispersion and significantly less particles agglomeration and the well-defined grain boundaries are noted. Fine surface features are visible in S4, although the SEM-derived dimensions should not be directly equated with the XRD crystallite size. The combined effect of surfactant addition and calcination modifies particle morphology and aggregation behavior.

3.3. Elemental Composition and Purity Analysis (EDAX)

The elemental analysis and purity verification of the as prepared SnO_2 nanoparticles is shown in Fig. 4 and the elemental analysis of synthesized SnO_2 nanoparticles can be found as quantitative elements analysis in Table 1. In the EDAX analysis spectra of all the samples we found typical features corresponding to elements of Sn (with L-line features as seen in 3.44 keV (Lα), 3.65 keV (Lβ), etc., and a strong K-line at 25.27 keV) and O peak with K-line (Kα) feature seen in 0.525 keV; that corroborate formation of SnO_2 nanostructure. Sn:O atomic ratios in all samples are close to the nominal stoichiometric ratio of 1:2 for SnO_2, with minor deviations that may arise from surface adsorbates and the semiquantitative nature of EDS analysis (Davar et al. 2010). It should be noted that, C (at ~ 0.277 keV) and N (at ~ 0.392 keV) elements appear with low proportions, but these elements contents change greatly among the different samples prepared under the different synthesis conditions. The carbon can be attributed to adsorbed CO_2 on the surface, to any remnant of residual organic

content of the surfactants, which have been used (Triton X-100) and to stray carbon signal coming from the vacuum in the SEM chamber. Nitrogen (N) could originate from adsorption of residue ammonia from the precipitating agent NH_4OH that was either entrapped within the particles structure or remained at the particle surface after extensive Washing. S3 showed the lowest detected carbon and nitrogen contents among the samples. This observation of elemental peaks for Sn, O and trace impurities may be associated with the washing procedure and the surfactant-assisted synthesis, although the present EDS data do not by themselves establish the mechanism responsible for the observed difference (Davar et al. 2010). However, S4 which was prepared with surfactant and then has been calcined to high temperatures contains moderate impurities where even if residual materials have been effectively removed in the calcined stage some parts of carbon from air also ware introduced. Similar thing is applicable to S1 which has high proportion of impurities because of less effective removal due to densely packed clusters (Davar et al. 2010). It makes more amount of impurities such as chlorine and ammonia to remain inside due to lack of complete access to washing solution into tightly packed mass. Hence even after calcination (which results in the partially decomposition of most residual organic ingredients, and residual hydroxide components), it does not improve the contamination of sample.

The O/Sn atomic ratios range from 1.84 to 1.86, slightly below the nominal stoichiometric value of 2.0. Overall, the EDS results are consistent with SnO_2 as the major elemental composition, while the small deviations should be interpreted considering the semiquantitative nature and surface sensitivity of EDS.

Table 1
Elemental Composition of SnO_2 Nanoparticles from EDAX Analysis.

Sample	Sn (at%)	O (at%)	C (at%)	N (at%)	O/Sn Ratio
S1	33.5	62.1	3.2	1.2	1.85
S2	34.2	63.5	1.8	0.5	1.86
S3	34.8	64.1	0.6	0.5	1.84
S4	34.5	63.8	1.1	0.6	1.85

3.4. Raman Spectroscopy Analysis

Raman spectroscopy was employed to investigate the vibrational properties and structural ordering of the synthesized SnO_2 nanoparticles. the room-temperature Raman spectra of all four samples (S1-S4) recorded in the range of 0-5000 cm^{-1} are displayed in Fig. 5 displays. The Raman spectra show distinct peaks characteristic of the tetragonal rutile structure of SnO_2. According to group theory analysis, rutile SnO_2 (space group D_4h^{14}, $P4_2/mnm$) possesses 15 optical phonon modes at the centre of the Brillouin zone, with the following irreducible representation (Diéguez et al. 2001; Katiyar et al. 1971).

$$\Gamma = 1A^1g + 1A^2g + 1A^2u + 1B^1g + 1B^2g + 2B^1u + 1E^1g + 3E^2g + 2E^1u + 4E^2u \quad (3)$$

The Raman active modes are: A_1g, B_1g, B_2g, E_1g, and E_2g. The spectra of all samples exhibit three main peaks at approximately 475 cm^{-1} (E_2g), 635 cm^{-1} (A_1g), and 775 cm^{-1} (B_2g), which are characteristic of the rutile SnO_2 phase. These assignments are consistent with previously reported values for SnO_2 nanoparticles

(Diéguez et al. 2001; Karmaoui et al. 2018). The E_2g mode at ~ 475 cm^{-1} corresponds to the vibration of oxygen atoms in the plane perpendicular to the c-axis and is sensitive to oxygen vacancy concentration (Bonu et al. 2015). The A_1g mode at ~ 635 cm^{-1} arises from the symmetric stretching of Sn-O bonds along the c-axis, while the B_2g mode at ~ 775 cm^{-1} is attributed to the asymmetric stretching of Sn-O-Sn bonds (Fazio et al. 2012; Bonna et al. 2026). The well-defined peaks corroborate the formation of the phase-pure rutile SnO_2, in agreement with the XRD result.

It is noteworthy to make the following remarks from the Raman study:

1. 1. Peak intensities: Sample S3 gave higher overall Raman intensity, especially at the E2g mode at ∼476 cm with intensity 150 a.u., demonstrating the good quality and degree of crystal order of rutile structure. The higher Raman intensity of S3 indicates a stronger Raman response under the present measurement conditions; however, Raman intensity alone should not be used as a direct measure of crystallinity or porosity.
2. 2. Peak positions and shifts: Small shifts in Raman-band positions among the samples indicate changes in the local vibrational environment that may be associated with crystallite size, strain, and defect-related disorder. The E_2g band shifts from 474.5 cm^{-1} in S1 to 476.0 cm^{-1} in S3, while the A_1g band shifts from 634.8 to 636.2 cm^{-1}. These shifts should be interpreted qualitatively because Raman peak position alone does not permit quantitative determination of oxygen-vacancy concentration.
3. 3. Relative intensities ratios: In addition, the I_{475}/I_{635} ratio may serve as a qualitative indicator of changes in defect-related Raman response and ranges between 1.0–6.0 among different samples. In terms of ratio in these samples, S3, S4, S1, and S2 have higher ratios in the order 6.0, 4.0, 2.0, 1.0, respectively. The higher ratio observed for S3 suggests a stronger defect-related Raman contribution; however, this ratio should not be interpreted as a direct quantitative measure of surface-defect or oxygen-vacancy concentration. The higher ratio observed for S3 indicates a stronger defect-related Raman contribution; however, direct enhancement of ROS generation was not measured in the present study.
4. 4. Peak broadening: The E_2g and A_1g modes show comparatively broader features in S1 and S2. Such broadening can be associated with smaller crystallite size, strain, and structural disorder, consistent with the XRD results. The comparatively sharper features in S3 and S4 indicate differences in structural ordering under the present synthesis conditions.
5. 5. Additional features: A weak feature around 545 cm^{-1} present in all samples may be associated with disorder-activated scattering or surface-related vibrational features (Hong et al. 2016).

Raman scattering investigation provides data that complement those obtained from XRD and SEM characterizations and support our conclusion on the strong impact of synthesis procedure on the order and the chemical-defect content of the synthesized SnO_2 nanomaterial. The Raman results complement the XRD and SEM observations and indicate that the synthesis conditions influence the structural and defect-related characteristics of the SnO_2 nanoparticles. A direct causal relationship between these characteristics and the biological response requires further investigation.

Table 2
Raman Peak Positions and Intensities for SnO_2 Nanoparticles.

Sample	E_2g (~ 475 cm^{-1})	A_1g (~ 635 cm^{-1})	B_2g (~ 775 cm^{-1})	Intensity Ratio (I_{475}/I_{635})
S1	474.5 (100)	634.8 (50)	775.2 (20)	2
S2	475.2 (50)	635.5 (50)	776.0 (25)	1
S3	476.0 (150)	636.2 (25)	776.8 (25)	6
S4	475.8 (100)	635.8 (25)	776.5 (20)	4

3.5. Surface Chemistry and Functional Groups

The chemical composition and functional groups on the synthesized SnO_2 nanoparticles were studied through the FTIR spectroscopy. All the four samples are taken for FTIR analyses in the region of 400–4000 cm^{-1} and shown in Fig. 6 along with their observed adsorption bands and assignment (Kar et al. 2011). As shown in Fig. 6, all four samples exhibit absorption bands associated with surface hydroxyl groups, adsorbed water, organic residues, and Sn–O-related vibrations. The broad band around 3308 cm^{-1} can be assigned to O–H stretching of surface hydroxyl groups and adsorbed water molecules (Boonpai et al. 2020). The O-H in bending modes appear as a weak absorption peak at 1415 cm^{-1} and is most active in sample S3, which may be correlated with the high surface area and porous structure. Some organically remaining functional groups were proved from absorption peaks at 2153 cm^{-1} (-C-C stretch, Alkyne) a weak absorption and at 1634 cm^{-1} (-C = O Stretch, Carboryl/carboxylate) a medium adsorption that are found to be more in samples that used surfactants (S3 and S4) as expected from original molecules.

The SnO-O-Sn stretching mode that may be attributed to the terminal Sn-O modes are observed at 1120 cm^{-1}, 623 cm^{-1} and another group with multiple bands with low intensity at 423 cm^{-1}, 403 cm^{-1} and 383 cm^{-1} (due to difference in geometry of surface atoms and coordination environments for tin atoms with more and less oxygen neighbours along bridging Sn-O-Sn and/or along terminal bonds (383–623 cm^{-1}). Those signals are sharp for the ordered case S3 and S4 while S1 and S2 are broadening and exhibit the two clearly spaced bands with small features in low intensity in the region of bridging modes for these surfaces that indicate that they may contain more disorder in the surface structure. Dehydroxylation of calcined materials at 600°C reduced the intensity of bands attributed to hydroxyl vibration (Lavalley et al. 2000) as expected and it seemed that organic residues may be present even upon treatment at 600°C due to strong surface binding of carbonaceous species. The major Sn–O-related vibrational features are present in all samples, thus confirming SnO structural purity.

3.6. Photoluminescence Spectroscopy

The Photoluminescence (PL) spectroscopy provides valuable insight into the defect states of metal oxide nanoparticles, particularly the presence and concentration of oxygen vacancies. the room-temperature PL emission spectra recorded at an excitation wavelength of 325 nm is shown in Fig. 7. The spectra exhibit broad emission bands in the visible region with multiple peaks indicating the presence of various defect states. In SnO_2, oxygen vacancies are

the most common and important point defects existing in three different charge states depending on electron occupancy: neutral V_o^0 (trapped two electrons, shallow donor), singly ionized V_o^+ (paramagnetic), and doubly ionized V_o^{2+} (deep donor) (Kar et al. 2011; Bonu et al. 2015). The formation of oxygen vacancies is energetically favourable in SnO_2 due to their relatively low formation energy of approximately 2–3 eV (Rahimi et al. 2024; Guan et al. 2026). The PL spectra of SnO_2 nanoparticles typically show emission bands in the visible region that can be deconvoluted into several Gaussian components corresponding to different defect states. The emission peaks at approximately 420–430 nm (2.95–2.88 eV) are assigned to neutral oxygen vacancies (V_o^0). The PL spectra of the four samples show distinct differences in emission intensities providing valuable information about the relative concentrations of different defect states.

Sample S1 exhibits the highest PL intensity overall with strong emissions across all wavelengths from 350 to 450 nm, reaching a maximum intensity at 361 nm. The high PL intensity indicates a high concentration of oxygen vacancies consistent with its uncalcined state. The presence of neutral and ionized vacancy states contributes to the broad emission observed, with the dominance of the 350–370 nm emission suggesting that neutral oxygen vacancies are the most abundant defect species. Samples S3 and S4 show that the addition of Triton X-100 surfactant appears to reduce oxygen vacancy concentration. The surfactant may promote more controlled nucleation and growth leading to fewer defect sites. However, the presence of organic residues on the surface, confirmed by FTIR analysis, may also passivate some emission centres. The combination of Triton X-100 and calcination does not effectively reduce defect states; rather, the surfactant may introduce additional emission centres. The presence of carbonaceous residues from the surfactant, even after calcination, may contribute to additional defect-related emissions and counteract the beneficial effects of thermal treatment.

The order of oxygen vacancy concentration based on PL intensity is: S1 > S4 > S2 > S3. This order correlates well with the antibacterial and anticancer activity, suggesting that while oxygen vacancies are important for ROS generation, an optimum concentration is required for maximum biological activity. The lower defect concentration in S3 appears to be beneficial for its enhanced biological performance.

3.7. Thermal Stability and Decomposition Behaviour

TGA of all four synthesized SnO_2 nanoparticle samples is represented by Fig. 8, carried out from room temperature to 1000^o C. Each TGA profile indicates two major regions of weight loss. Below 150^o C occurs removal of physically adsorbed water (sample S2 displayed the highest value of 4.2% while S3 displayed lowest of 0.8%). From 150^o to 300^o C an intermediate weight loss region appears due to decomposition of the residues of organic matter, the weight loss values are higher for surfactant assisted samples S3 & S4 as there might be presence of even higher contents of carbon based deposits than sample S1 & S2 respectively. Above 300^o C in all four samples there are no signs of weight loss and they show superior thermal stability (Patel et al. 2021; Davar et al. 2010). Thus it can be concluded that total weight loss followed the order S2(5.2%)> S1 (2.0%) > S4 (1.8%)> S3 (1.1%) showing high thermal stability of S3. These results are found to corroborate well with the higher purity of sample S3 (shown by EDAX), better crystal structure (XRD) and low concentration of oxygen vacancies (PL). The samples S3 and S4 having high thermal stability would be useful in biomedical applications, since they could retain their original structures during processes of sterilization & storage.

3.8. Antibacterial Activity

The antibacterial actions of the developed samples S1, S2, S3 and S4 were investigated against six bacteria strains namely- Escherichia coli, Staphylococcus aureus, Pseudomonas aeruginosa, Klebsiella pneumoniae, Bacillus subtilis and Vibrio cholerae by a well diffusion technique using positive reference material of Gentamicin (160 µg). The obtained activities are detailed below in Table 3 and Fig. 9.

From the screened values against different bacterial strains described in Table 3, the tested Samples S1 showed weak inhibition on S. aureus (9 mm) and V. cholerae (8 mm), but did not show effect on other organisms, S2 is weak activity K. pneumoniae (11 mm) and V. cholera (8mm), Sample S3 showed activity on S. aureus (8 mm) & K. pneumonia (11 mm), Sample S4 showed inhibition against K. pneumonia (12 mm). However, K.pneumonia exhibited highest inhibition by S2, S3, and S4 bacteria whereas E. coli, P. aeruginosa and Bacillus spp., were resistant against all samples. These result demonstrate that all synthesized SnO_2 nanoparticles possessed weak specific antibacterial properties and may require some further studies on purification or concentration or combined approach for enhance antimicrobial performance. This result may be due to moderate oxygen vacancy concentrations on the surfaces of samples

which were previously discussed as it indicates that controlling synthesis condition to enhance the surface properties may improve ROS-mediated antibacterial efficacy.

The antibacterial mechanism may be associated with surface generated oxidative stress and reactive oxygen species, similar to that reported for other metal oxide nanomaterials, but ROS and specific damage were not directly monitored in this study. Based on this zone-of-inhibition data, no defined trend emerged between gram-positive and gram-negative bacteria. The strain-dependent trends from the data indicate future research may focus on surface modification, concentration optimization or combination with existing antimicrobial agents.

3.9. Anticancer Activity

Our cytotoxic results on SKMEL melanoma cell line indicate the presence of significant cell viability differences in potency with the samples at different doses. Table 4 shows the percentage cell viability, while the calculated IC_{50} value is given in Table 5 for various concentrations. S1 exhibited poor cytotoxicity with the cell viability approximately 79% even at the highest evaluated concentration 100 µg/mL. The cytotoxicity of S2 increased with increasing concentrations in the dose-dependent manner and reached cell viability 67% at 100 g/mL, with no IC being reached under the range studied. S3 caused considerable reduction in cell viability (cell viability approx. 50% at 100 µg/mL) with IC of 95.57 µg/mL and the most cytotoxic was S4 (IC = 66.96 µg/mL and cell viability decreased to 41.27% at 100 µg/mL). Overall cytotoxicity activity order was S4 > S3 > S2 > S1.The dose-dependent response observed for S3 and S4 indicates increasing cytotoxicity with increasing nanoparticle concentration. The present MTT assay demonstrates reduced cell viability but does not by itself establish a specific apoptotic or mitochondrial mechanism.

The IC50 values derived in the present work are found to be in good correlation with the relatively wide ranges of the results obtained with some other metal-oxide and plant mediated nanoparticles. It is not possible to make a direct comparison with published data due to the variation in cell types used, duration of exposure, assay parameters, nanoparticle preparation and treatments used. For example, plant-mediated Ag nanoparticles showed lower IC50 value toward MCF-7 cell as much as (Sivalingam et al. 2026), plant-

originated ZnO nanoparticles demonstrated IC50 between approximately 53–62 µg/mL and showed cytotoxicity on A549 cell lines (Said et al. 2026). Moderate cytotoxicity also revealed from biosynthesized AgCl nanoparticles against cancer cell lines (Eltayeb et al. 2025). These comparisons indicate that the biological response of SnO_2 nanoparticles is strongly dependent on both material characteristics and experimental conditions.

Table 3
Zones of Inhibition (mm) for SnO_2 nanoparticles against bacterial strains.

Type	Bacteria	Zone of Inhibition (mm)				
		Gentamycin (160 µg)	S1	S2	S3	S4
Gram-Positive	Staphylococcus aureus	27	9	-	9	-
	Bacillus subtilis	28	-	-	-	-
Gram-Negative	Escherichia coli	32	-	-	-	-
	Pseudomonas aeruginosa	26	-	-	-	-
	Klebsiella pneumoniae	23	-	11	11	12
	Vibrio cholerae	25	8	8	-	-

The reported IC_{50} values of CuO nanoparticles synthesized via solution combustion using Flemingia strobilifera biomass against K562 and HepG2 cells were 94.82 and 79.63 µg/mL, respectively (Tejaswini et al. 2026). The S4 IC_{50} value of 66.96 µg/mL is within the broad range reported for several plant-mediated nanomaterials, although direct comparisons should be made cautiously because of differences in cell models and experimental protocols. The present study does not establish reduced toxicity, enhanced biocompatibility, or a selective mechanism because no normal-cell control was included. The higher cytotoxicity observed for S4 may be associated with differences in morphology, surface chemistry, and defect-related properties.

4. CONCLUSION

SnO_2 nanoparticles were conveniently synthesized by co-precipitation via a facile solution-route with tin (□) chloride dihydrate as the starting material, in the presence or absence of the Triton X-100. Structural characterizations of the synthesized samples (XRD, SEM-EDS, FTIR, Raman, PL, TGA) showed that all of the samples exhibit typical tetragonal rutile phase (of SnO) and their average crystallite sizes were calculated ranging from 14.5 to 23.0 nm. The synthesis conditions influenced the observed morphology and degree of aggregation.

Surfactant-assisted synthesis (S3 and S4) produced more textured and less agglomerated morphologies than the non-surfactant samples. EDS confirmed Sn and O as the major detected elements, with minor C and N signals. FTIR indicated surface OH functional groups and Sn-O related vibrations, while Raman indicated typical rutile SnO_2 modes at ~ 475, ~635, and ~ 775 cm. Variations in Raman as well as PL spectra reflect changes in defect levels among the samples, whereas these two techniques do not yield oxygen vacancies concentrations. TGA showed the lowest total weight loss for S3 (1.1%) under the experimental conditions.

Biological evaluation revealed that all synthesized compounds exhibit very poor and strain-dependent antibacterial activity, with K. Pneumoniae presented the most susceptible strain. The SKMEL melanoma cell-line assay showed a decreased cell viability, dependent on the concentration, where the lowest IC (66.96 µg mL^{-1}) was experimentally found for S4 (95.57 µg mL^{-1}) followed by S3. For S1 and S2, the IC was not reached within the tested range, and they are reported as > 100 µg mL^{-1}.

These structure-activity relationships indicate that a structure surface-defect related response might be influencing the biological activity. The IC_{50} values obtained for S3 and S4 indicate moderate cytotoxicity within the tested concentration range. Their biological potency remains lower than that of several conventional chemotherapeutic agents

This study reports a simple co-precipitation route for preparing SnO_2 nanoparticles and demonstrates concentration-dependent cytotoxicity against SKMEL melanoma cells together with weak, strain-dependent antibacterial activity. These findings provide a basis for further investigation of SnO_2 nanoparticles for biomedical applications

Declarations

Conflicts of Interest

The authors declare no conflicts of interest.

Author Contribution

Author ContributionsDr. N.Krishnamoorthy: conceptualization, methodology, data curation, investigation, writing original draft, supervision; Ms. K. Indhumathi: validation, review and editing; Dr. A.Gladya Anusha: formal analysis, project administration, review and editing. All authors have read and approved the final version of the manuscript.

Data availability

The data that support the findings of this study are available from the corresponding author upon reasonable request.

References

1. Agadi NP, Korgaonkar K, Mathad AS, Seetharamappa J (2023) Green synthesis of SnO2-β-cyclodextrin graphene oxide composite for electrochemical sensing of an antioxidant drug, alpha lipoic acid. Ionics 29:1593–1603
2. Akter S, Madhuvilakku R, Kar AK, Nila IS, Liu P, Inuzuka H et al (2026) Reactive oxygen species (ROS) in cancer: from mechanism to therapeutic implications. Signal Transduct Target Ther 11:111

3. Alamdari A (2026) Efficient photocatalytic oxidation of nitrogen containing compounds of fuel over heterojunctions under visible light irradiation: Photocatalysts classification, process parameters, kinetics, and mechanisms. Results Eng 30:111188
4. Alzahrani B, Elderdery AY, Alzerwi NAN, Alsrhani A, Alsultan A, Rayzah M et al (2023) Pluronic-F-127-Passivated SnO2 Nanoparticles Derived by Using Polygonum cuspidatum Root Extract: Synthesis, Characterization, and Anticancer Properties. Plants 12:1760
5. Anil A, Bindhu D, Sreekala CO (2024) Synthesis, structural, morphological and optical characterization of tin oxide nanoparticles and its application as an oxide layer in MOS capacitor. AIP Conf Proc 3171(1):020004. https://doi.org/10.1063/5.0223687
6. Azam A, Ahmed AS, Habib SS, Naqvi AH (2012) Effect of Mn doping on the structural and optical properties of SnO2 nanoparticles. J Alloys Compd 523:83–87
7. Balakrishnan K, OICC Author (2024) Synthesis and characterization of SnO2 nanoparticles by Co-Precipitation method. Int J Nano Dimens 12(1)
8. Bamagous GA, Ibrahim IAA, Alzahrani AR, Shahid I, Shahzad N, Falemban AH et al (2025) Multifunctional SnO_2-Chitosan-D-carvone Nanocomposite: A Promising Antimicrobial, Anticancer, and Antioxidant Agent for Biomedical Applications. J Inorg Organomet Polym Mater 35:3111–3127
9. Bamisaye A, Adekola MA, Abati SM, Etafo NO, Ademola OS, Joseph PT et al (2025) Recent advances in metal/metal-oxide nanoparticle-polymer nanohybrid for biomedical applications. Mater Today Chem 49:103086
10. Billik P, Čaplovičová M (2009) Synthesis of nanocrystalline SnO2 powder from SnCl4 by mechanochemical processing. Powder Technol 191:235–239
11. Bonna SK, Swapna EJ, Hoimontee TI, Ahmed F, Khandaker JI (2026) Synthesis and characterization of SnO2 nanoparticles using an autoclave-assisted hydrothermal method. Next Mater 13:102654
12. Bonu V, Das A, Amirthapandian S, Dhara S, Tyagi AK (2015) Photoluminescence of oxygen vacancies and hydroxyl group surface functionalized SnO 2 nanoparticles. Phys Chem Chem Phys 17:9794–9801
13. Boonpai S, Wannakao S, Suriye K, Márquez V, Panpranot J, Jongsomjit B et al (2020) Influence of surface Sn species and hydrogen interactions on the OH group formation over spherical silica-supported tin oxide catalysts. React Chem Eng 5:1814–1823
14. Chandrasekaran K, Kokkarachedu V, Sisubalan N, Vijayan A, Hendry Moses P, Edison Raj Godwin P et al (2024) Exploring the Medical Applications of SnO2 Nanomaterials: Antimicrobial, Antiviral, and Anticancer Therapies, pp 227–242
15. CLSI (2020) Performance standards for antimicrobial susceptibility testing. CLSI supplement M100, 30th edn. Clinical and Laboratory Standards Institute, Wayne, PA
16. D'Souza A, Kurale RS, Kumar D, Rakesh P, Kumar R (2025) Recent Advances and Developments in Transition Metal Oxides Synthesis, Functionalization, and Biomedical Applications. Bionanoscience 15:408
17. Dalapati GK, Sharma H, Guchhait A, Chakrabarty N, Bamola P, Liu Q et al (2021) Tin oxide for optoelectronic, photovoltaic and energy storage devices: a review. J Mater Chem A 9:16621–16684
18. Das TR, Meena M, Potheher IV, Udhaya PA (2020) Hydrothermal Synthesis and Characterization of Tin Oxide (SnO2) Nanoparticles. J Environ Nanotechnol 9(2):15–19.

https://doi.org/10.13074/jent.2020.06.202408

19. Davar F, Salavati-Niasari M, Fereshteh Z (2010) Synthesis and characterization of SnO2 nanoparticles by thermal decomposition of new inorganic precursor. J Alloys Compd 496:638–643
20. de Conti MCMD, Dey S, Pottker WE, La Porta FA (2023) An overview into advantages and applications of conventional and unconventional hydro(solvo)thermal approaches for novel advanced materials design. Mater Today Sustain 23:100458
21. Dharmaraja AT (2017) Role of Reactive Oxygen Species (ROS) in Therapeutics and Drug Resistance in Cancer and Bacteria. J Med Chem 60:3221–3240
22. Diéguez A, Romano-Rodríguez A, Vilà A, Morante JR (2001) The complete Raman spectrum of nanometric SnO2 particles. J Appl Phys 90:1550–1557
23. Eltayeb BMA, Elshazly EH, Aboelmagd HA, Zidan SAH, Mohamed AKSH (2025) Sustainable production of silver chloride nanoparticles from desert flora for biomedical applications with multifunctional biological activities. Sci Rep 15:32674
24. Fatima F, Verma SR, Pathak S, Gaur A (2021) Antibacterial assessment of metal oxide nanoparticles using agar well diffusion method against clinical bacterial pathogens. Chem Pap 75(12):6415–6425. https://doi.org/10.1007/s11696-021-01811-y
25. Fazio E, Neri F, Savasta S, Spadaro S, Trusso S (2012) Surface-enhanced Raman scattering of SnO2 bulk material and colloidal solutions. Phys Rev B 85:195423
26. Gebreslassie YT, Gebretnsae HG (2021) Green and Cost-Effective Synthesis of Tin Oxide Nanoparticles: A Review on the Synthesis Methodologies, Mechanism of Formation, and Their Potential Applications. Nanoscale Res Lett 16:97
27. Gour A, Kumar P (2021) Co-precipitation synthesis and characterization of SnO_2 nanoparticles for structural and optical properties. Chem Pap 75(8):4101–4110. https://doi.org/10.1007/s11696-021-01642-x
28. Guan L, Jiang Y, Zhao F, Yang L, Bibi B, Liu Y et al (2026) Oxygen vacancy modulation in SnO_2 thin films for enhanced photoelectrochemical performance via defect engineering. Appl Surf Sci 719:164970
29. Hong SN, Kye YH, Yu CJ, Jong UG, Ri GC, Choe CS et al (2016) Ab initio thermodynamic study of the SnO 2 (110) surface in an O 2 and NO environment: a fundamental understanding of the gas sensing mechanism for NO and 2. Phys Chem Chem Phys 18:31566–31578
30. Hossain N, Mobarak MH, Mimona MA, Islam MA, Hossain A, Zohura FT et al (2023) Advances and significances of nanoparticles in semiconductor applications – A review. Results Eng 19:101347
31. Hughes KJ, Ganesan M, Tenchov R, Iyer KA, Ralhan K, Diaz LL et al (2025) Nanoscience in Action: Unveiling Emerging Trends in Materials and Applications. ACS Omega 10:7530–7548
32. Hussain I, Bibi A, Khail MIK, Zhenbo T, Khan R, Hussain Z et al (2025) Advancing environmental remediation: Mechanistic insights into SnO_2-based photocatalysts for organic pollutant degradation and microbial inactivation. J Water Process Eng 77:108511
33. Imlay JA (2013) The molecular mechanisms and physiological consequences of oxidative stress: lessons from a model bacterium. Nat Rev Microbiol 11:443–454

34. John N, Somaraj M, Tharayil NJ (2018) Synthesis, Characterization and Anti – Bacterial Activities of SnO2 Nanoparticles Using Biological Molecule. IOP Conf Ser Mater Sci Eng 360:012007
35. Kamaraj I, Kamaraj S, Shanmugam G (2025) Emerging strategies and multifunctional applications of nanomaterials in modern nanomedicine. Med Nov Technol Devices 28:100400
36. Kar A, Kundu S, Patra A (2011) Surface Defect-Related Luminescence Properties of SnO 2 Nanorods and Nanoparticles. J Phys Chem C 115:118–124
37. Karmaoui M, Jorge AB, McMillan PF, Aliev AE, Pullar RC, Labrincha JA et al (2018) One-Step Synthesis, Structure, and Band Gap Properties of SnO 2 Nanoparticles Made by a Low Temperature Nonaqueous Sol–Gel Technique. ACS Omega 3:13227–13238
38. Kashyap A, Chakraborty B, Siddiqui MS, Tyagi H, Kalita H (2023) Selective and Sensitive Detection of Formaldehyde at Room Temperature by Tin Oxide Nanoparticles/Reduced Graphene Oxide Composite. ACS Appl Nano Mater 6:7948–7959
39. Katiyar RS, Dawson P, Hargreave MM, Wilkinson GR (1971) Dynamics of the rutile structure. III. Lattice dynamics, infrared and Raman spectra of SnO 2. J Phys C Solid State Phys 4:2421–2431
40. Kebede MA (2020) Tin oxide–based anodes for both lithium-ion and sodium-ion batteries. Curr Opin Electrochem 21:182–187
41. Khan I, Ragab AH, Alraih AM, Al-Mhyawi SR, Ullah A, Hussain H et al (2025) Properties and Biomedical Applications of SnO2-Based Nanomaterials; Future Perspectives and Challenges. J Clust Sci 36:217
42. Kharbanda J, Priya R (2022) Synthesis and applications of tin oxide nanoparticles: An overview. Mater Today Proc 68:916–921
43. Kishorwara R, Devika PS, Madhumitha M, Mohanprasanth A, Snega R (2026) Structural and optical characteristics of green-synthesized ZnO/SrO nanocomposites using pomegranate peel extract and their biological activity. Next Mater 12:102006
44. Kumar A, Maan D, Jain K, Jain SK, Tripathi B (2025) A comprehensive review on synthesis methods, photodegradation mechanisms, and diverse applications of tin oxide (SnO2) nanoparticles. J Lumin 288:121584
45. Lavalley J-C, Lamotte J, Busca G et al (2000) NOx adsorption onto dehydroxylated or hydroxylated tin dioxide surface. Application to SnO_2-based sensors. Sens Actuators B 65:288–292
46. Leblanc E, Périer-Camby L, Thomas G, Gibert R, Primet M, Gélin P (2000) NOx adsorption onto dehydroxylated or hydroxylated tin dioxide surface. Application to SnO_2-based sensors. Sens Actuators B Chem 62:67–72
47. Lan X, Xiong X, Liu J, Yuan B, Hu R, Zhu M (2022) Insight into Reversible Conversion Reactions in SnO2-Based Anodes for Lithium Storage: A Review. Small 18:2106740
48. Li Z, Zeng W, Li Q (2022) SnO2 as a gas sensor in detection of volatile organic compounds: A review. Sens Actuators Phys 346:113845
49. Liang Q, Liu X, Zeng G, Liu Z, Tang L, Shao B, Zeng Z, Zhang W, Liu Y, Cheng M, Tang W, Gong S (2019) Surfactant-assisted synthesis of photocatalysts: Mechanism, synthesis, recent advances and environmental application. Chem Eng J 372:429–451. https://doi.org/10.1016/j.cej.2019.04.168

50. Manimaran M, Muthuvel A, Said NM (2023) Microwave-assisted green synthesis of SnO2 nanoparticles and their photocatalytic degradation and antibacterial activities. Nanotechnol Environ Eng 8:413–423
51. Masuda Y (2022) Recent advances in SnO2 nanostructure based gas sensors. Sens Actuators B Chem 364:131876
52. Mohanta D, Ahmaruzzaman M (2016) Tin oxide nanostructured materials: an overview of recent developments in synthesis, modifications and potential applications. RSC Adv 6:110996–111015
53. Nasir Z, Shakir M, Wahab R, Shoeb M, Alam P, Khan RH et al (2017) Co-precipitation synthesis and characterization of Co doped SnO 2 NPs, HSA interaction via various spectroscopic techniques and their antimicrobial and photocatalytic activities. Int J Biol Macromol 94:554–565
54. NavaneethaKrishnan S, Rosales JL, Lee KY (2019) ROS-Mediated Cancer Cell Killing through Dietary Phytochemicals. Oxid Med Cell Longev 2019:1–16
55. Patel GH, Chaki SH, Kannaujiya RM, Parekh ZR, Hirpara AB, Khimani AJ et al (2021) Sol-gel synthesis and thermal characterization of SnO2 nanoparticles. Phys B Condens Matter 613:412987
56. Pathak C, Sharma A, Verma R (2020) Quantitative energy dispersive X-ray microanalysis using standard ZAF matrix correction procedure for nanostructure oxides. Vacuum 177:109381. https://doi.org/10.1016/j.vacuum.2020.109381
57. Rahimi K, Rawal A, Zhu YF, Hart JN, Lovell EC, Scott J (2024) Defect engineering in SnO2 catalysts for the organic oxidation reaction. Appl Catal B Environ Energy 359:124515
58. Rahman M (2025) Tin oxide thin films for the future: A paradigm shift in property engineering for advanced functional devices. Next Mater 9:101341
59. Sagadevan S, Lett JA, Fatimah I, Lokanathan Y, Léonard E, Oh WC et al (2021) Current trends in the green syntheses of tin oxide nanoparticles and their biomedical applications. Mater Res Express 8:082001
60. Said AH, Shaibah F, Moustafa M, Elamary RB (2026) Harnessing plant extracts for zinc oxide nanoparticles: a greener route to enhanced biocompatibility and therapeutic potential. J Sol-Gel Sci Technol 117:47
61. Shanmugasundaram A, Munirathinam K, Lee DW (2024) SnO2 nanostructure-based acetone sensors for breath analysis. Micro Nano Syst Lett 12:3
62. Sharma A, Ahmed A, Singh A, Oruganti SK, Khosla A, Arya S (2021) Review—Recent Advances in Tin Oxide Nanomaterials as Electrochemical/Chemiresistive Sensors. J Electrochem Soc 168:027505
63. Shinde VR, Revi N, Murugappan S, Singh SP, Rengan AK (2022) Enhanced permeability and retention effect: A key facilitator for solid tumor targeting by nanoparticles. Photodiagnosis Photodyn Ther 39:102915
64. Silva C, Oliveira M, Santos R (2016) Structural, optical and FTIR characterization of tin dioxide nanostructures for chemical sensing. Chem Pap 70(11):1485–1494. https://doi.org/10.1515/chempap-2016-0089
65. Sivalingam AM (2026) Green synthesis of silver nanoparticles (AgNPs) using swietenia macrophylla extract evaluation of their antioxidant, antimicrobial, and cytotoxic activity against MCF-7 breast cancer cells. J Mol Struct 1353:144710

66. Sultana S, Islam MT, Rahman MA (2023) Structural phase analysis and crystallite size determination of tin oxide nanoparticles using Debye-Scherrer method. Appl Nanosci 13(4):2891–2899. https://doi.org/10.1007/s13204-022-02688-4
67. Sun C, Yang J, Xu M, Cui Y, Ren W, Zhang J et al (2022) Recent intensification strategies of SnO2-based photocatalysts: A review. Chem Eng J 427:131564
68. Tejaswini A, Raveesha HR, Vasudha DR, Dhananjaya N, Mylarappa M (2026) Combustion synthesis and characterization of Flemingia strobilifera plant part mediated CuO nanoparticles for biological studies. Next Res 102112
69. Tripathy A, Mohanty S, Nayak SK (2022) Sample preparation methodologies and morphological investigation of oxide nanoparticles by scanning electron microscopy. Micron 154:103201. https://doi.org/10.1016/j.micron.2021.103201
70. Üstünel T, Ide Y, Kaya S, Doustkhah E (2023) Single-Atom Sn-Loaded Exfoliated Layered Titanate Revealing Enhanced Photocatalytic Activity in Hydrogen Generation. ACS Sustain Chem Eng 11:3306–3315
71. Van Acker H, Coenye T (2017) The Role of Reactive Oxygen Species in Antibiotic-Mediated Killing of Bacteria. Trends Microbiol 25:456–466
72. Vidhu VK, Philip D (2014) Catalytic and antibacterial activities of SnO_2 nanoparticles synthesized using Sorghum vulgare seed extract. Plant Sci Today 1(2):62–67. https://doi.org/10.14719/pst.2014.1.2.18
73. Wali Q, Fakharuddin A, Jose R (2015) Tin oxide as a photoanode for dye-sensitised solar cells: Current progress and future challenges. J Power Sources 293:1039–1052
74. Wang HW, Wesolowski DJ, Proffen TE, Vlcek L, Wang W, Allard LF et al (2013) Structure and Stability of SnO 2 Nanocrystals and Surface-Bound Water Species. J Am Chem Soc 135:6885–6895
75. Wang J, Umezawa N, Hosono H (2016) Mixed Valence Tin Oxides as Novel van der Waals Materials: Theoretical Predictions and Potential Applications. Adv Energy Mater 6:1501190
76. Zhao C, Wang C, Qiu Y, Wang Z, Yao G, Yang R (2023) The mechanism and preparation of nano-SnO2@fly ash antistatic composite powder. Powder Technol 430:119003
77. Zhao Q, Ma L, Zhang Q, Wang C, Xu X (2015) SnO2-Based Nanomaterials: Synthesis and Application in Lithium-Ion Batteries and Supercapacitors. J Nanomater 2015:832947
78. Zhao YF, Sun YP, Yin X, Yin GC, Wang XM, Jia FC et al (2018) Effect of Surfactants on the Microstructures of Hierarchical SnO2 Blooming Nanoflowers and their Gas-Sensing Properties. Nanoscale Res Lett 13:250

Figures

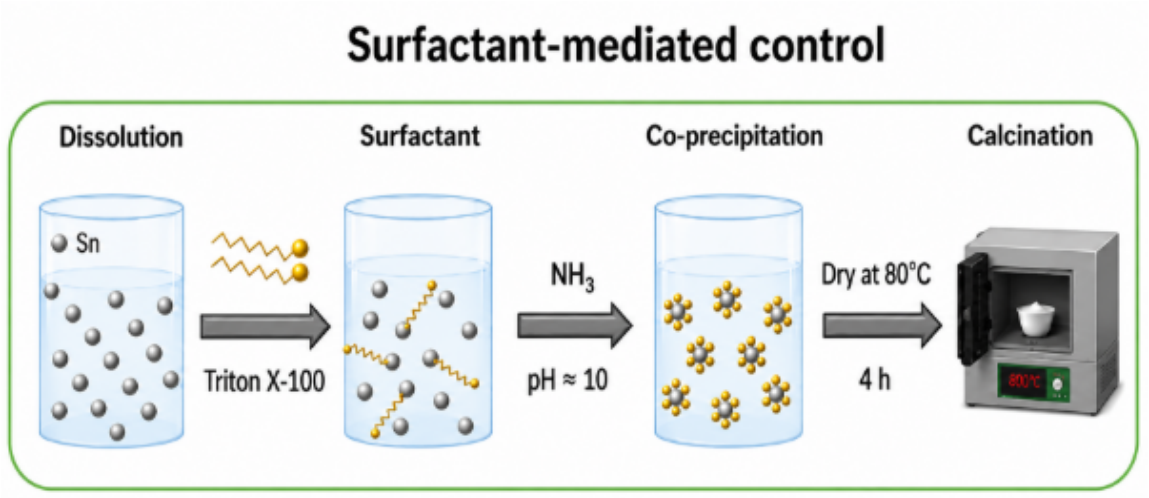


Figure 1

Surfactant-mediated synthesis of SnO_2 nanoparticles using Triton X-100.

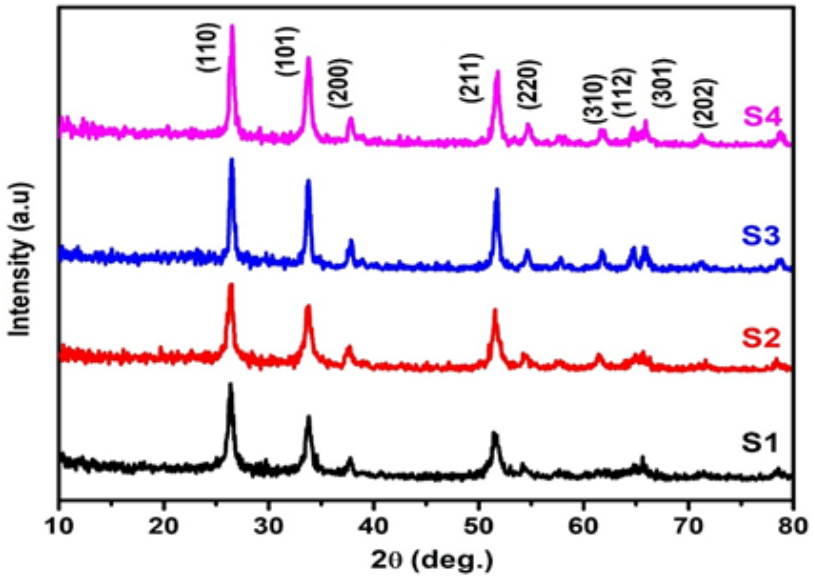


Figure 2

XRD patterns of SnO_2 nanoparticles (S1-S4) showing characteristic peaks of tetragonal rutile structure

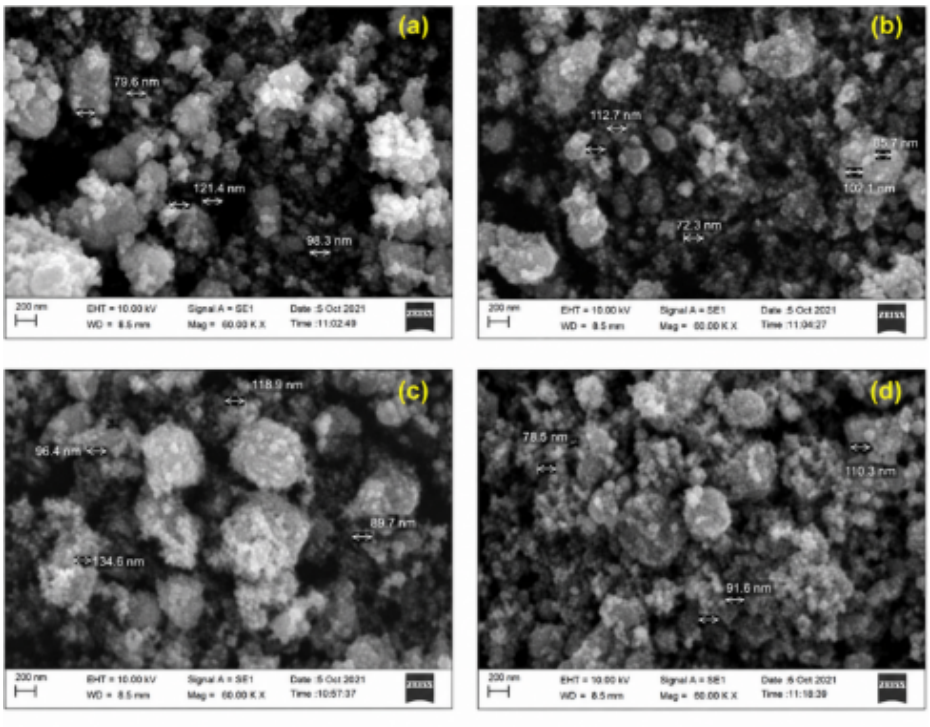


Figure 3

SEM images of SnO_2 nanoparticles: (a) S1, (b) S2, (c) S3, (d) S4.

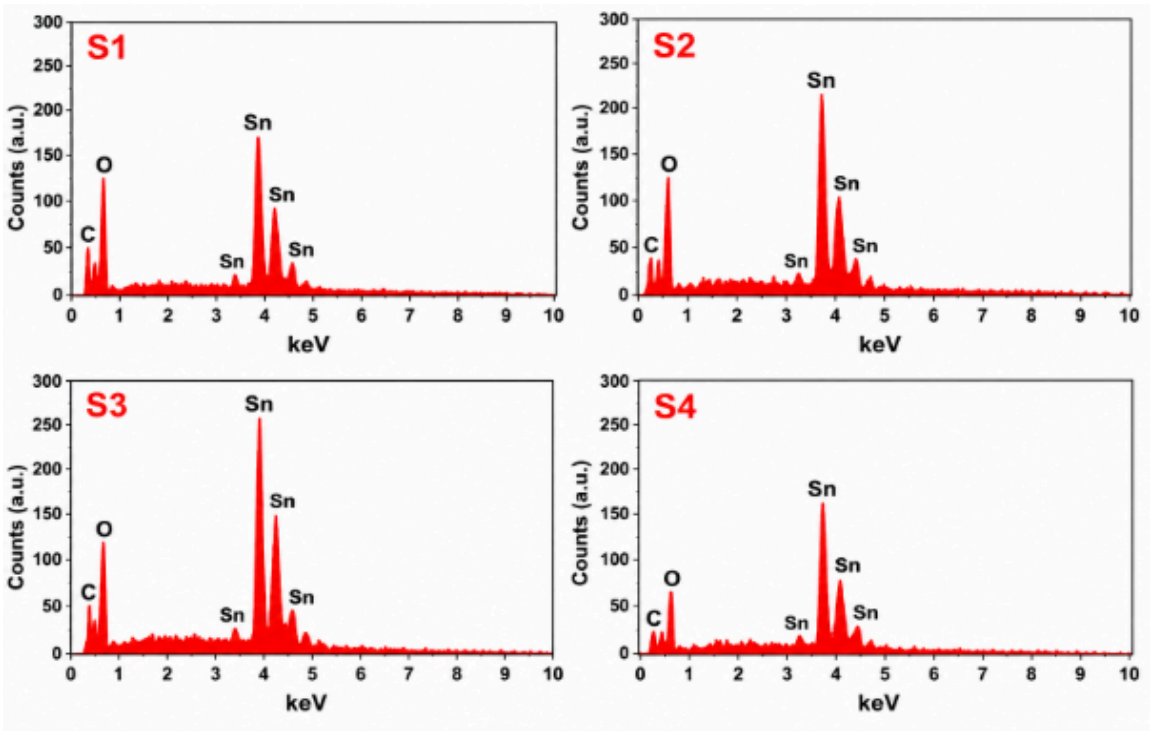


Figure 4

EDAX spectra of SnO_2 nanoparticles: (a) S1, (b) S2, (c) S3, (d) S4 showing elemental peaks for Sn, O and trace impurities.

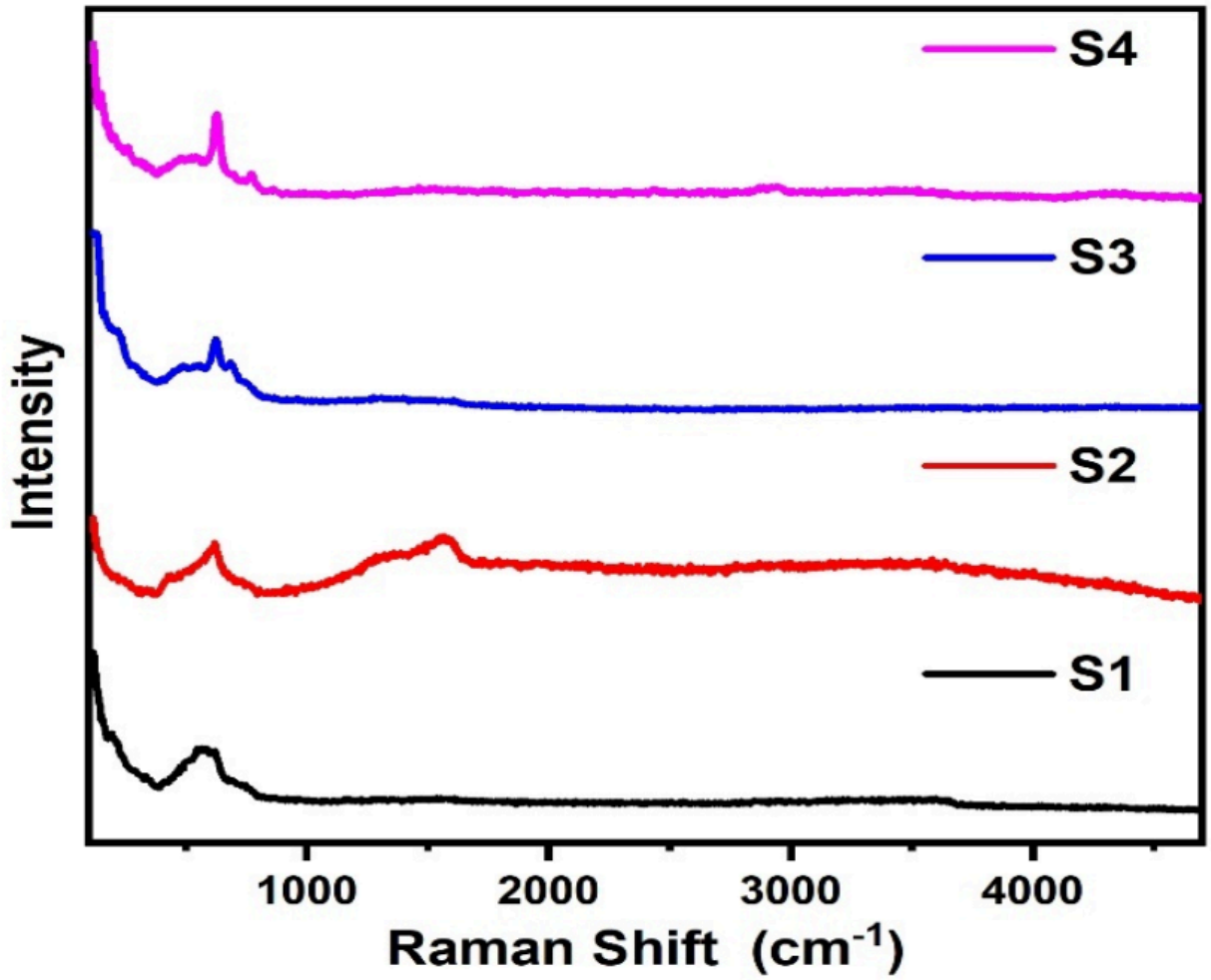


Figure 5

Raman spectra of SnO_2 nanoparticles (S1-S4).

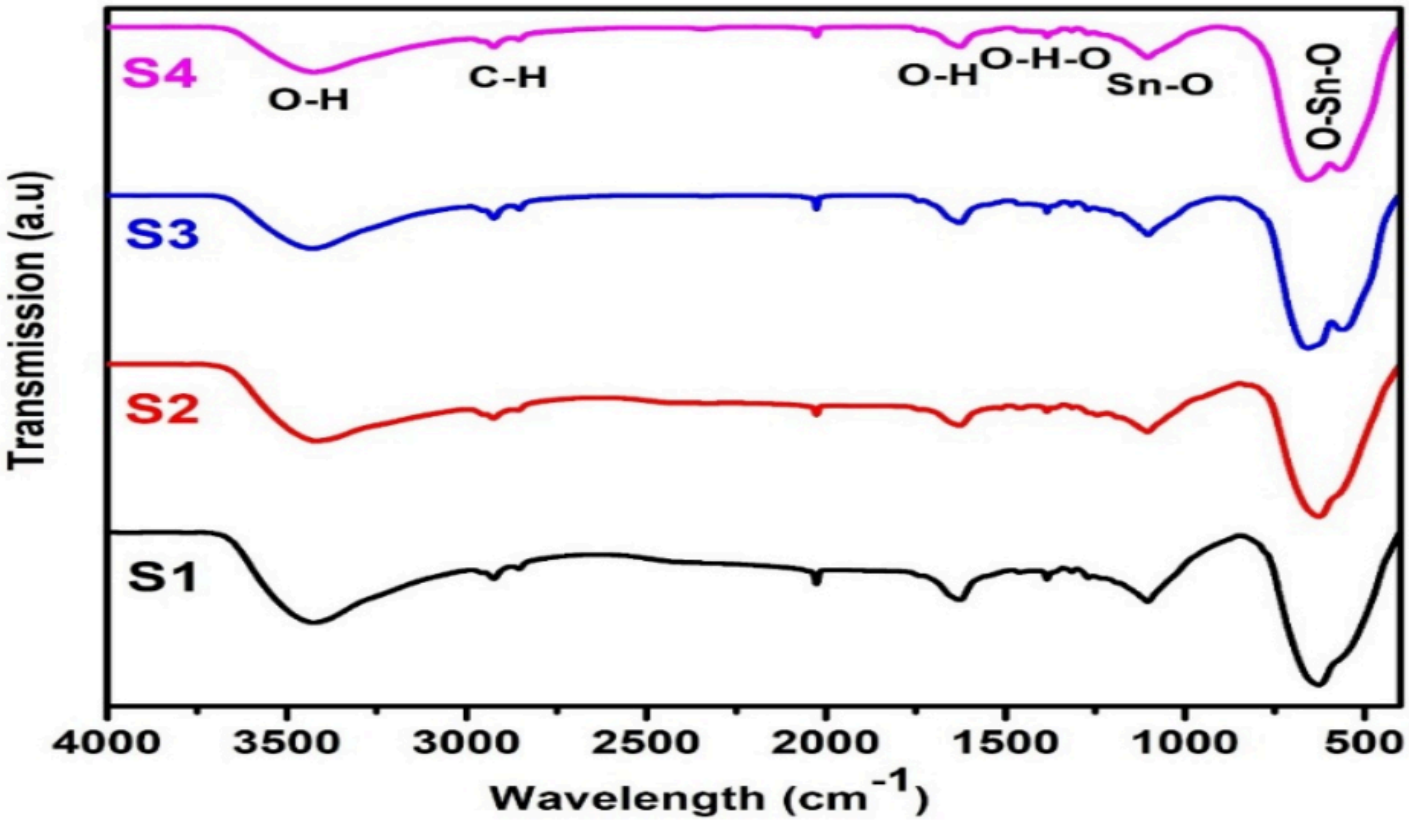


Figure 6

FTIR spectra of SnO_2 nanoparticles (S1-S4) showing characteristic absorption bands.

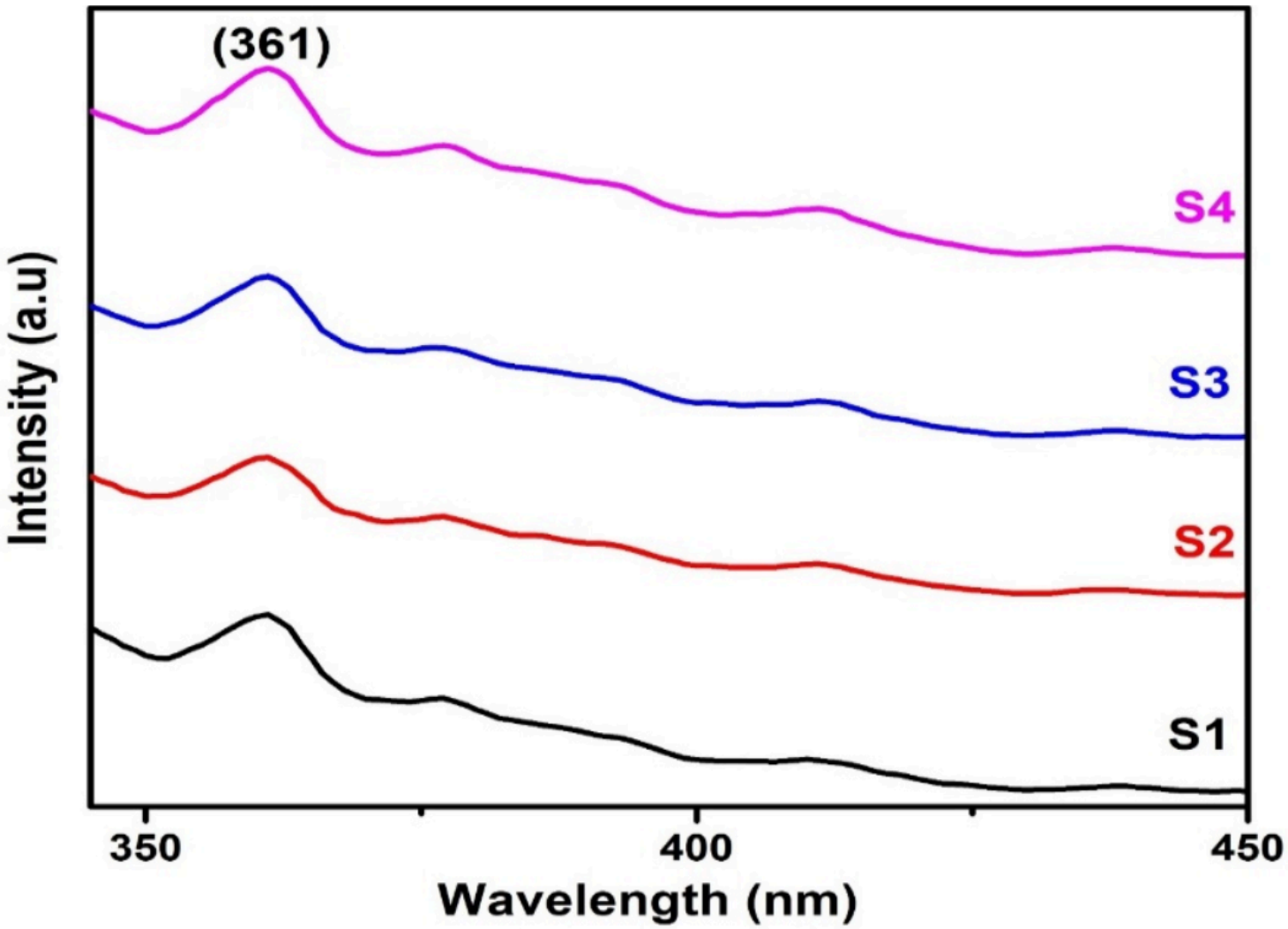


Figure 7

PL emission spectra of SnO_2 nanoparticles (S1-S4) at λ_{ex} = 325 nm.

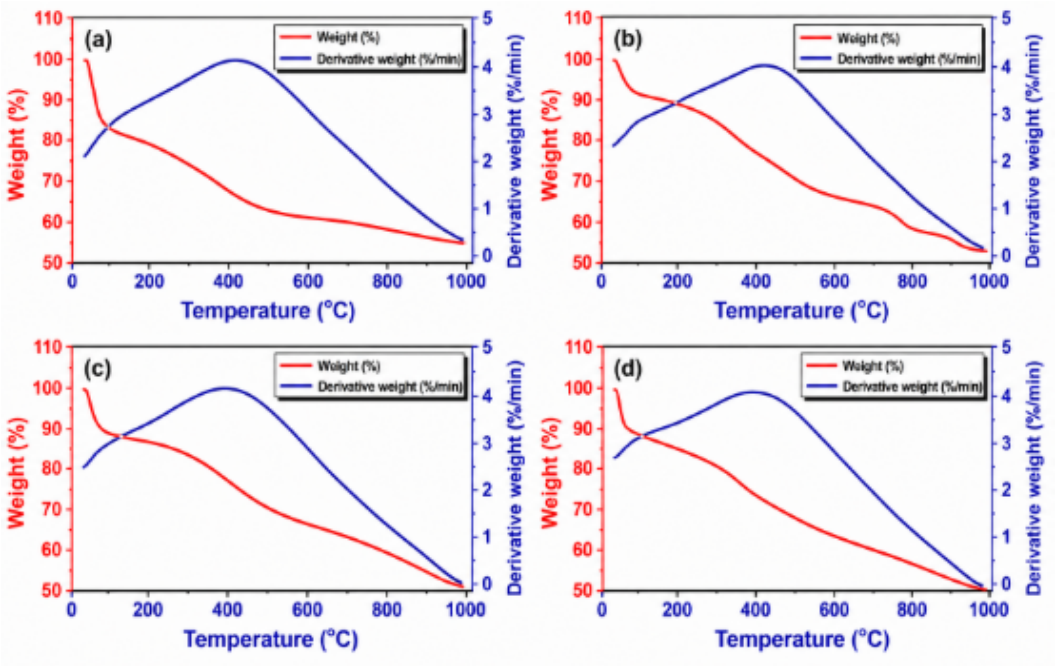


Figure 8

TGA curves of SnO_2 nanoparticles (S1-S4) showing weight loss as a function of temperature.

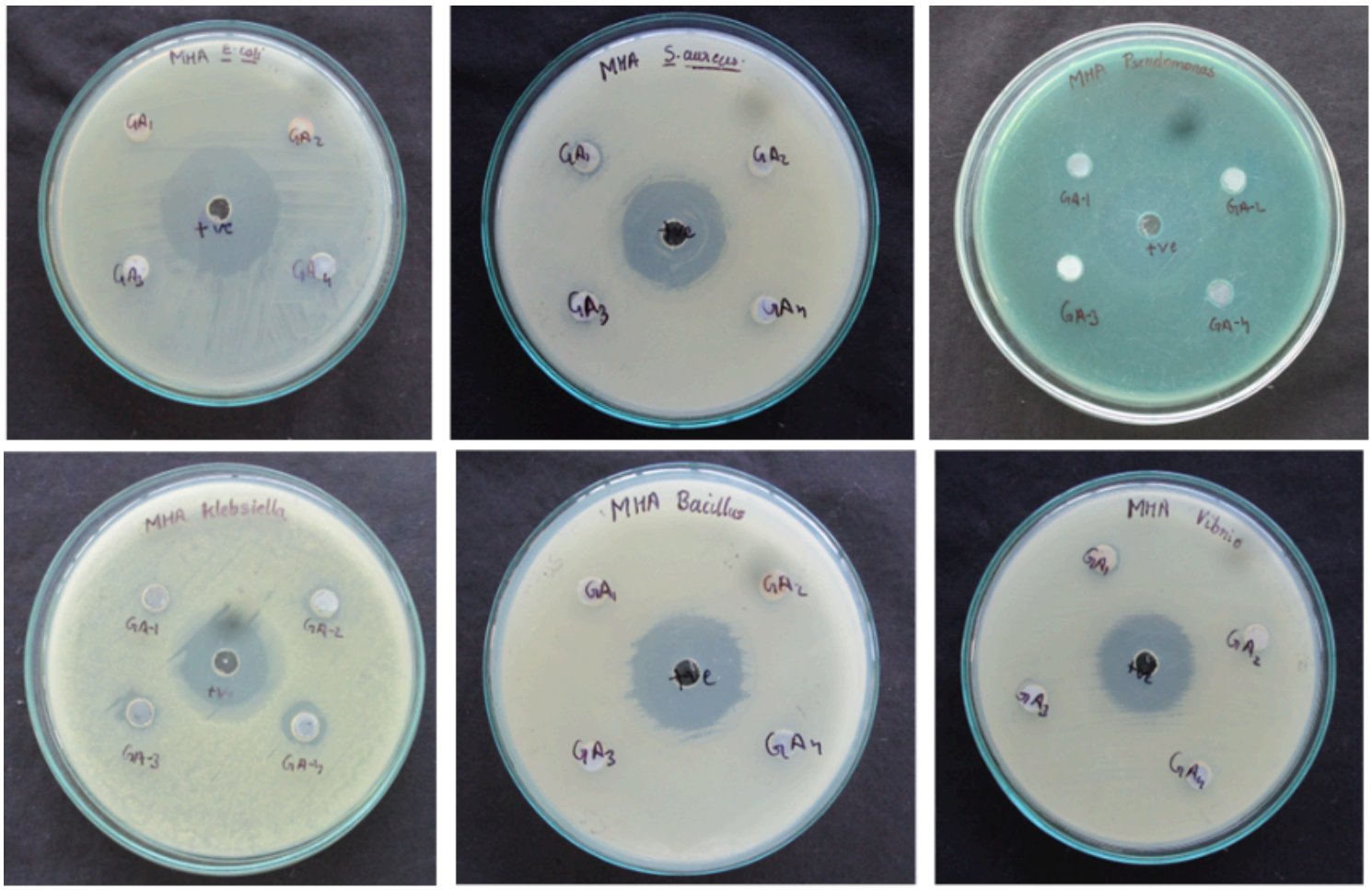


Figure 9

Antibacterial activity of *SnO_2 nanoparticles* against (a) S. aureus, (b) B. subtilis, (c) E. coli, (d) P. aeruginosa, (e) K. pneumoniae, and (f) V. cholera.